Numerical analysis of the mechanical role of the ribs in groin vaults

G. Lengyel[a,*], K. Bagi[a]

[a]*Budapest University of Technology and Economics, Department of Structural Mechanics, 1111 Budapest, Műegyetem rkp. 3, Hungary*

Abstract

The role of ribs in the mechanical behaviour of masonry cross vaults has been the subject of intense debates since the 19th century. Literature on the subject diverges from considering the ribs as the main load-bearing units which carry the weight of the masonry web, to the opinion that the ribs are merely decorations. This research focused on the simplest type of cross vaults, i.e. groined vaults formed by the intersection of two semicircular cylindrical mid-surfaces. Instead of the widely used Limit State Analysis which is reliable only if specific conditions are satisfied, discrete element modelling (the commercial code 3DEC, based on an explicit time integration scheme), and a classical finite element code (ANSYS) was applied in the investigations. In the applied DEM code (3DEC) the elements (corresponding to the voussoirs) may slide along each other, and can be separated from their neighbours in any directions; and new contacts may be formed between them, in a computationally efficient automatized manner.

Keywords: DEM, masonry cross vault, masonry

1. Introduction

The application of ribbed vaults appeared in Europe already in the 10th century, presumably for Muslim or Armenian inspiration [1]. The idea became widespread in the late Romanesque era, and then became a fundamental feature of Gothic structures. In Christian architecture the ribs are rather thick and strong in comparison to the thin, dense, decorative networks of the seemingly fragile ribs of Arabic vaults; consequently, their mechanical function is also different. In the present paper we shall focus on the former ones, specifically on the earliest version of ribbed vaults which became widely applied throughout Europe, i.e. late Romanesque groin vaults. The interested reader can find a detailed overview and discussion on the hypothesis about the possible origins of ribbed vaulting, with an emphasis on the Islamic version, in [1].

Early Romanesque cross vaults consisted of two semicircular barrel vaults, usually intersecting at a right angle. To build such a vault, a complex system of scaffolding and centring had to be erected in order to define the shape of the intrados and lay the masonry. For larger spans this made the construction process rather complicated and inconvenient. In addition, in such structures the intersection lines formed by the two surfaces (i.e. the diagonal groins) were rather weak and attracted damages.

An efficient solution came into general use in Europe from approximately the 12th century. Along the planned intersection lines ashlar ribs were erected first, which then played the role of permanent centring, during construction as well as through the lifetime of the structure. The masonry shell was divided into smaller domains this way, which made the construction process easier and larger spans could consequently be overcome; in addition, the ribs also had an aesthetic effect. This solution was proven definitely successful and quickly spread about, then became a main characteristic of Gothic architecture in the following centuries.

*Corresponding author

Email addresses: lengyelg@mail.bme.hu (G. Lengyel), kbagi@mail.bme.hu (K. Bagi)

Regarding Gothic ribbed vaults, a fundamental question has been under debate since the 19th century: are the ribs the main load-carrying members and the masonry shell is mostly a passive load on it, or on the contrary, the masonry web carries its own weight and the ribs only provide an additional reinforcement and a visual impression of stability. Huerta [2] gave a thorough overview on that debate, from the early hypothesis (e.g. Willis, [3] who made a distinction between "mechanical ribs" sustaining the vault and "decorative ribs" applied mainly for aesthetic functions) till sophisticated numerical investigations (e.g. Barthel, [4]). Based on the Safe Theorem of plastic limit state analysis applied to masonry structures (Heyman, [5]), Huerta pointed out that the question itself was wrong: since the internal force system in a masonry structure is extremely sensitive to slight changes in the geometrical boundary conditions: small soil settlements or leaning of supporting walls, etc. may abruptly change the stress distribution which was valid under previous circumstances, and it means that either the ribs or the masonry shell, or both of them in a variable proportion, may therefore be the main load-bearing component, depending on the current conditions of the structure, subjected to change continously. This conclusion is, of course, also valid for Romanesque ribbed vaults.

However, the question of structural functions of the rib, i.e. the differences between the mechanical behaviour of unribbed and ribbed vaults, remained an open issue. According to Heyman [5] the ribs resolve those stress concentrations which would otherwise occur around the four corners where the vault is supported from below. Alexander et al [6] found that the ribs strengthen the vault just along its weakest lines. Other, still unrevealed effects may also be present. The aim of the present study is therefore to provide numerical simulation and comparison of the behaviour of unribbed and ribbed cross vaults carrying their self-weight during different displacement histories of their boundaries. The aim is not to find "the current state" of stress for a given geometry and supports: instead, our intention is to survey the set of those possible states which occur for a wide spectrum of disturbed boundary positions, and find out what differences are caused by the existence of the ribs both in the stress states and in the failure modes.

The numerical investigations presented in the paper focus on the simplest and earliest type of ribbed vaults, shown in Figure 1: two semicircular barrel vaults having equal radius, intersecting above a square plan.

Several different computational tools exist for the analysis of masonry behaviour. They can be categorized into three main groups.

- Limit State Analysis methods (e.g. Thrust Network Analysis, Block & Ochsendorf [7]) have a limited validity if they are based on the assumption that frictional sliding does not occur. Those models which allow for the possibility of failure with frictional sliding (e.g., Livesley [8], [9]; Orduña & Lourenço, [10]; D'Ayala & Tomasoni, [11]) are definitely more suitable for our purposes, though they are computationally rather expensive.
- Continuum-based techniques like, e.g., the finite element method (FEM) may provide valuable insight into the behaviour of the structure, but those versions which are most suitable for the analysis of the failure regime (nonlinear FEM with no-tension constitutive behaviour, or application of contact elements reflecting Coulomb-type behaviour at pre-defined surfaces) are also rather inefficient from computational point of view. Thus, in our researches FEM was applied only for that farly limited range of the behaviour where linear elasticity could be assumed. The results obtained this way are valid only for tension-resisting states of the structure, and should be accepted with reservations. However, the sophisticated output systems and visualization possibilities offered by recent commercial software packages can significantly contribute to the understanding of the internal state of the analyzed structure; this is why we did not completely exclude FEM from the analysis.
- Discrete element modelling (DEM) considers the structure as a collection of separate blocks each of which is able to move and deform independently of each other. The blocks may come into contact with each other where contact forces are transmitted, causing stresses and deformations inside the blocks. The blocks may also frictionally slide along each other. The contact creation, sliding and separation is automatically followed in a computationally efficient manner in DEM. These characteristics make

DEM particularly suitable for masonry analysis; before, during and after failure, and this is why we chose DEM to serve as the main tool of the investigations.

There were several methodological differences between the FEM and DEM models applied in the present paper. The FEM model was based on compiling and solving the global equilibrium equations of a quasi-static system according to the usual displacement method: $\mathbf{Ku} = \mathbf{f}$, where $\mathbf{f}$ was the vector of forces reduced to the nodes of the finite elements, $\mathbf{u}$ was the basic unknown, i.e., the displacement vector that moved the system from the initial unloaded geometry to the final equilibrium state corresponding to the external forces acting on the structure (some of these displacements were prescribed in the case of support displacement analysis); and $\mathbf{K}$ was the global stiffness matrix describing the geometrical and material data of the simulated structure.

The DEM analyses were based on simulating the motions of the individual nodes of the discrete elements in time, with the help of an explicit time integration of Newton's force-acceleration law: $v_{i+1/2} = v_{i-1/2} + \frac{f_i}{m}\Delta t$, where v denotes the velocities, Δt is the length of the finite time step considered, m is the mass assigned to the analyzed node, and f_i is the force resultant reduced to that node (see details in Section 4.1.1). In other words, the discrete elements were subdivided into regions belonging to the different nodes, and their motion was followed in time. The main differences between the applied FEM and DEM technique were the following:

- The FEM solution was time-independent, only small displacements could be analyzed, while DEM was able to produce finite (i.e. large) displacements received from a series of small incremental time steps.
- FEM used a global stiffness matrix, while in the DEM code all individual nodes were considered independently, and the modification of the contact forces between the elements was not considered during a time step (contact forces were upgraded only after receiving the modified position of the nodes).
- The usual continuity conditions between adjacent elements were satisfied in the FEM model, while such conditions were not applied between the discrete elements in the DEM model.
- The topology of the structure remained the same in the FEM model, while the DEM model was able to consider contact separation or creation and sliding, so the topological modifications could be simulated throughout the successive time steps.

The novelties of this work were made possible by applying the discrete element tecnique, using which a more accurate numerical model could be built with appropriate boundary conditions to understand the force transmission process of cross vaults. This was a more realistic model which gave more reliable results on the system of the internal forces and on the cracking and sliding behaviour of the ribbed and unribbed vaults for self-weight and support displacements.

The paper is outlined as follows. Section 2 describes the geometrical and material characteristics of the simulated vaults. Section 3 focuses on FEM modelling while Section 4 introduces the DEM analysis. Section 5 compares the results and draws the main conclusions on the structural functions of the rib.

2. Description of the analyzed vaults

2.1. Geometry and material characteristics

A right-handed (x, y, z) global reference frame was applied to define the position of the points of the structural models. The middle surface of every simulated (unribbed and ribbed) quadripartite vault was formed by two semicircular barrels having the same 5 m radius, intersecting above a 10 m $*$ 10 m square plan (Figure 1). The thickness of the masonry shell was 200 mm in every case. In the discrete element models the vault and the ribs consisted of three-dimensional voussoirs. In the FEM analysis the masonry shell was modelled by a two-dimensional curved surface and the ribs were one-dimensional beam elements connected to the shell.

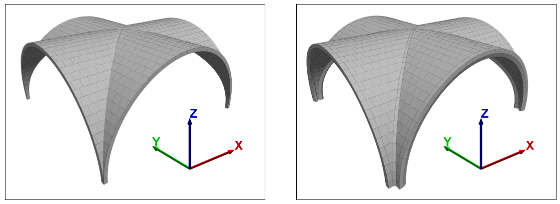

(a) (b)

Figure 1: Geometry of the simulated cross vaults: (a): Groin vault; (b): Ribbed vault

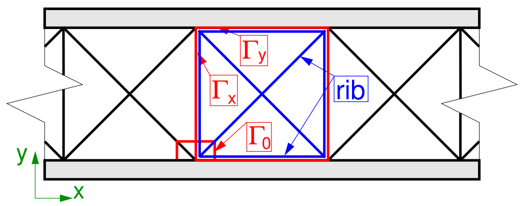

Figure 2: The analysed vault as a unit in a single-aisle church; notation of the boundaries

The simulated vault was imagined as being a unit of a complex single-aisle church (shown in Figure 2) and its connections with the adjacent structural components were reflected by applying proper boundary conditions on the analyzed cross vault. The boundaries Γ_0 corresponded to the supporting piers in the four corners; Γ_x expressed the effect of the adjacent cross vaults; finally, Γ_y played the role of the longitudinal walls of the nave. (The applied boundary conditions will be explained in Section 2.2 in more detail.)

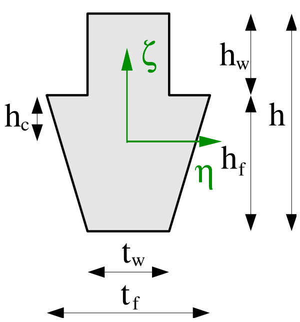

Figure 3: The cross section of the rib and its geometrical parameters

In the ribbed structures the ribs were placed along the diagonals and along the four sides of the square plan. The diagonal ribs had the same cross-section as the transverse and longitudinal ribs. Figure 3 shows the applied cross-section and its geometrical parameters. In order to analyze the effect of weak versus strong ribs, the simulations on the ribbed structures were done twice: with a thinner and then with a more robust, thicker rib; see Table 1 for the exact data. Here h_c determines the position of the centroid, measured from the upper edge of the flange.

Material parameters corresponding to travertine limestone were applied: Young modulus: $E = 14.8\,\mathrm{GPa}$; Poisson's ratio: $\nu = 0.2$; material density: $\rho = 2348\,\mathrm{kg/m^3}$ (Á. Török [12]). In the discrete element simulations the joints between voussoirs were considered to be dry so that there was no resistance against tension, and the friction angle, ϕ was set to 30°.

Model	h_w[mm]	h_f[mm]	h_c[mm]	h[mm]	t_w[mm]	t_f[mm]
Thin rib	200-280	200	5-(-39)	400-480	150	200
Thick rib	200-280	400	103-75	600-680	150	200

Table 1: Applied dimensions of the cross section of the rib

2.2. Boundaries

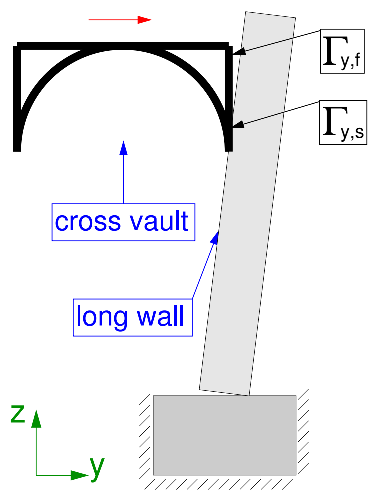

Figure 4: Lateral support of the vault and the two regions of the Γ_y boundary

The interaction between the analyzed quadripartite vault and the adjacent structural members was described with the help of the following three different boundaries (see Figure 2 again):

- The piers supporting the vault from below in the four corners were modelled with the perfectly fixed boundary Γ_0. In the FEM analysis they were point-like supports, while in the DEM simulations boundary Γ_0 consisted of finite areas (200 mm × 200 mm) corresponding to the cross-section of the supporting piers.
- The adjacent cross vaults were assumed to prevent any longitudinal (x-directed) translation of the points of the boundary Γ_x. For this reason, in the FEM analysis the rotations of the 2D shell gridpoints about the y axis were also set to zero along this boundary; in the DEM model (consisting of three-dimensional voussoir blocks) the x-directional nodal translations were set to zero along Γ_x.
- The lateral connection between the semicircular edge of the vault and the longitudinal wall (see Figure 4) was divided into two regions in the simulations, according to the general experience that cross vaults tend to be separated from the lateral walls of the nave. The lower part of the lateral arch ($\Gamma_{y,s}$) denotes the part where the edge of the vault is able to exert forces on the wall, and the upper part ($\Gamma_{y,f}$) is where the vault is separated from the wall bending outwards. The subdivision of Γ_y into this two mechanically different regions under self-weight (considering different wall thicknesses, heights) was analyzed with the help of discrete element simulations introduced in the Appendix. The results showed that approximately one quarter of the semicircular arc length remained in contact with the wall in the analyzed cases. Thus in all FEM and DEM tests the lower 2 m length of the lateral arcs were supported against y-directional translation (boundary $\Gamma_{y,s}$), while the upper region (boundary $\Gamma_{y,f}$) was free.

2.3. The loads

First the analyzed vault models were submitted to their self-weight only. Then starting from its equilibrium, two different types of quasi-static support displacements were tested by applying prescribed velocity histories on boundaries Γ_0 and $\Gamma_{y,s}$: in the first case, the piers and lateral walls were moved outwards; in the second case, the left piers and the connected wall were translated upwards while supports on the right hand side moved downwards.

3. Finite element analysis

3.1. The mechanical model

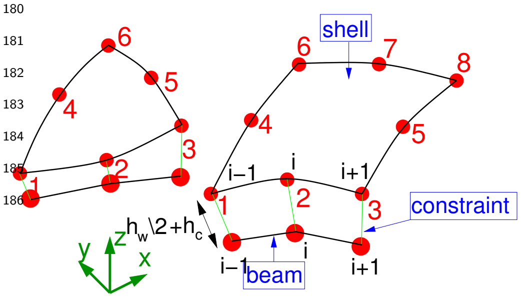

Figure 5: 6-node and 8-node shell elements applied in the FEM models; connection between the shell and the beam element

The finite element investigations were carried out with the help of ANSYS 14.5. The vault was modelled as a 2D-surface shell structure strengthened by 1D beam elements. Mindlin-Reissner shell elements ("SHELL-281") were applied in which the shear deformations were taken into account by a linear shear warping function. The elements had 6 or 8 nodes (see Figure 5), each node with three translational (u, v, w) and three rotational (ϕ_x, ϕ_y and ϕ_z) degrees

Boundary	u	v	w	ϕ_x	ϕ_y	ϕ_z
Γ_0	0	d_h	d_v	0	0	0
Γ_x	0	-	-	-	0	-
$\Gamma_{y,s}$	-	d_h	-	0	-	-
$\Gamma_{y,f}$	-	-	-	-	-	-

Table 2: Boundary conditions in the finite element simulations, self-weight plus prescribed horizontal (d_h) or vertical (d_v) support displacements

of freedom. The ribs were modelled with Timoshenko beam elements ("BEAM-188"), also with a linear warping function.

The connections between the nodes of the shell and the ribs were perfectly rigid for all degrees of freedom, see Figure 5. The geometry and material properties were described in Section 2.1.

The mechanical effect of the neighbouring structural elements were taken into account with suitably chosen boundary conditions, as explained in Section 2. In the FEM model the nodes on boundary Γ_x (corresponding to the adjacent cross vaults) were supported against longitudinal translation and against rotation about the transverse horizontal axis. The nodes on boundary Γ_0 (i.e., the piers) were perfectly fixed. The boundaries corresponding to the contacts with the lateral walls were divided into two subdomains $\Gamma_{y,s}$ and $\Gamma_{y,f}$ (see again Section 2 and also the Appendix): nodes on $\Gamma_{y,s}$ were fixed against transverse horizontal translation and against rotation about the longitudinal axis, while the nodes on $\Gamma_{y,f}$ were free. Table 2 summarizes the prescribed displacements on the boundaries.

3.2. *The analysed characteristics*

In order to quantify the mechanical state of the analyzed vault models, first a local frame (ξ, η, ζ) coordinate system has to be assigned to each point of the middle surface. Axis ζ is normal to the surface. Assuming that the masonry blocks are arranged such that the joint directions correspond to the x and y directions, the axes ξ and η are, by definition, tangent to the planar cuts determined by vertical planes with normals along x and y intersecting with the middle surface in the analysed point.

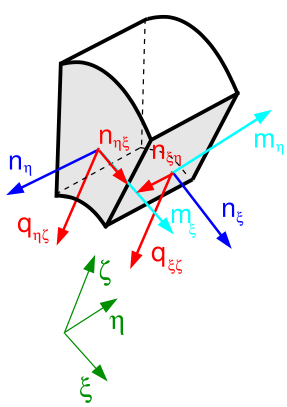

Figure 6: The analysed distributed internal forces and moments in the FEM model

The stresses, acting on the planes normal to ξ and η respectively, can be integrated along the thickness of the shell, and the usual internal forces of the Mindlin-Reissner theory (shown in Figure 6) are received. The normal forces n_ξ and n_η, the bending moments m_ξ and m_η, and the crosswise shear force components $q_{\xi\zeta}$ and $q_{\eta\zeta}$ will serve as the basis for the forthcoming characteristic quantities describing the statical state of the analyzed vaults. The in-plane shear force components and the torsional moments will not be analyzed in detail in the present paper since their contribution is not a characteristic reason for the loss of stability of cross vaults. However, the in-plane shear forces play an important role: based on the normal and the in-plane shear forces, the principal membrane forces.

A masonry vault may globally or locally lose its stability mostly because of *hinging*, *sliding* or *separating* of the joints between the voussoirs. Corresponding to these phenomena, the following characteristics were analysed in the FEM simulations:

- Mobilized friction ratio: $f[\%]$

$$f[\%] = max\left(\frac{q_{\xi\zeta}}{-n_\xi tan(\phi)}, \frac{q_{\eta\zeta}}{-n_\eta tan(\phi)}\right), \tag{1}$$

this quantity expresses how close the neighborhood of the analysed point is to the state when it slides out perpendicularly to the shell.

- Eccentricity of the internal forces: $e[\%]$

$$e[\%] = max\left(\frac{|m_\eta|}{-n_\xi \frac{h_w}{2}}, \frac{|m_\xi|}{-n_\eta \frac{h_w}{2}}\right), \tag{2}$$

as the value of e reaches 100%, the point of action of the resultant of normal stresses on the ξ or η plane reaches the intrados or the extrados. This quantity is not sensitive to whether a crack would open from below or from above, and whether the crack opens about the ξ or η axis, but its magnitude identifies those domains which are most endangered for hinging.

3.3. FEM analysis for self-weight with fixed supports

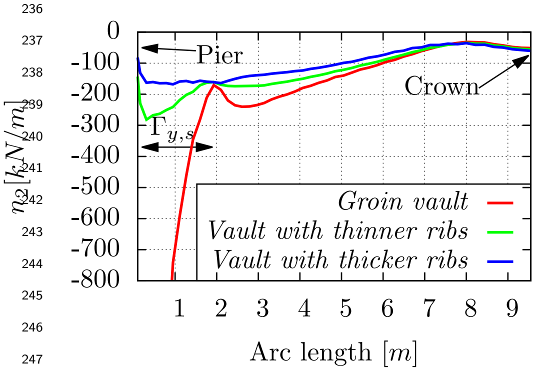

Figure 7: Characteristic membrane forces in the shell along the groin for self-weight, principal compression

The diagram in Figure 7 shows how the magnitude of the minimum principal membrane force varies along the diagonal groin. Without ribs, singularity occurs at the piers in the corners. This singularity is smoothened out by the ribs; the thicker are the ribs, the smaller are the peak forces. At the inner part of the groin, i.e. near the crown, the difference between ribbed and unribbed vaults is negligible. These results confirm Heyman's statements on that the ribs decrease the membrane force peaks around the piers.

The magnitude of the compressive principal force is shown in colors in Figure 8 (a-b-c). The red and yellow domains are those parts of the shell where even the highest compression is close to zero. Since the frictional resistance of the joints in a masonry depends on the magnitude of compression, these domains are particularly vulnerable for the blocks sliding out. The thicker are the ribs, the smaller these low-pressure regions are.

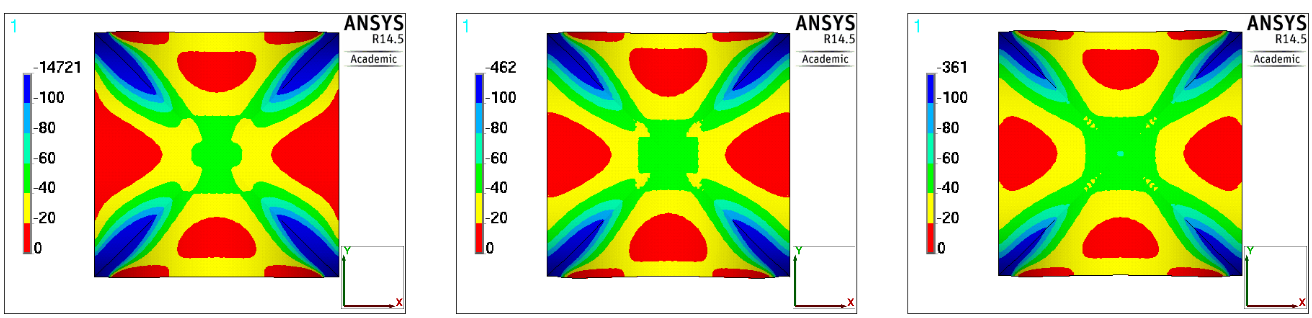

(a) (b) (c)

Figure 8: Magnitude of principal compression force along the vault surface for self-weight: (a) *Groin vault*, (b) *Vault with thinner ribs*, (c) *Vault with thicker ribs*

Figure 9 illustrates the eccentricity parameter. In the red domains the bending moment about axis ξ or η is so large that the resultant of the normal stresses is outside the shell thickness, hence in a real vault without considerable tensional resistance hinges would develop here. Without ribs (Figure 9 (a)) such a domain can be seen longitudinally along the crown. Additional analysis (not detailed here) gave the result that the direction of the vector of large moments is parallel to axis x, so a longitudinal hinge line would indeed be formed along the crown line. The endangered domains mostly disappear in the presence of ribs (Figures 9 (b) and 9 (c)).

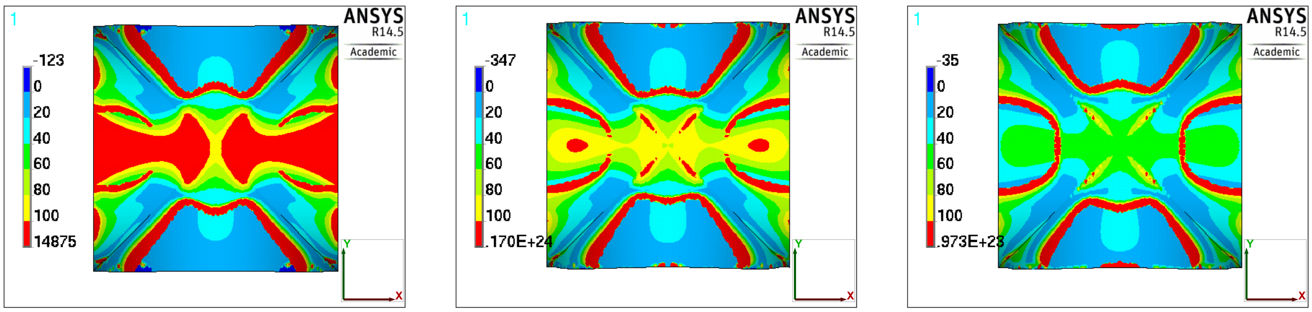

(a) (b) (c)

Figure 9: Magnitude of eccentricity along the vault surface for self-weight: (a) *Groin vault*, (b) *Vault with thinner ribs*, (c) *Vault with thicker ribs*

3.4. FEM analysis for self-weight and horizontal relative translations of the piers and lateral walls

In order to simulate that the longitudinal supports of a nave (the top of the lateral walls) slightly shift outwards, boundaries Γ_0 and $\Gamma_{y,s}$ of the FEM model were translated outwards so their distance from the longitudinal plane of symmetry was increased.

Figure 10 shows how the eccentricity varies along the longitudinal line of the crown. Very tiny support displacements significantly modify the position of the resultant. In the unribbed structure (Fig. 10 (a)) the resultant is practically everywhere outside the shell: in the case of a no-tension material, a hinge line would be formed along the crown. In the vault with thick ribs (Fig. 10 (b)) eccentricities are significantly smaller: under a 1 mm support separation (0.1% of the span) normal forces remain inside the shell thickness, and as the support separation increases, they remain inside the thickness in the regions around the ribs.

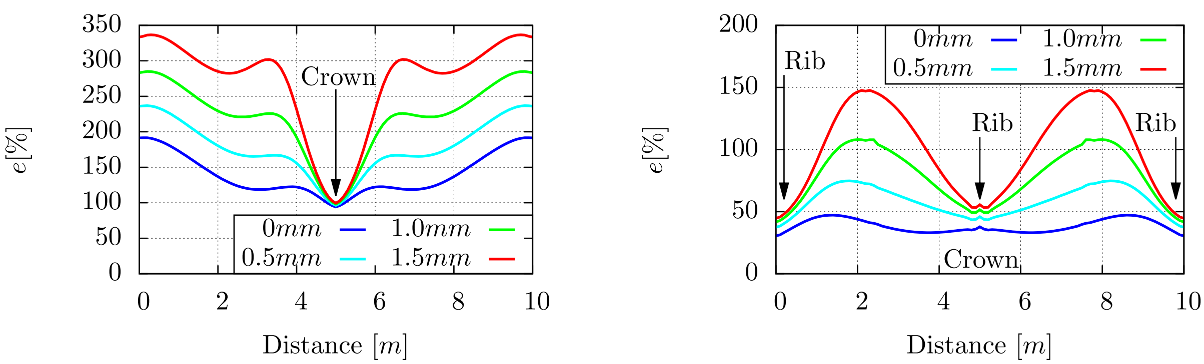

(a) (b)

Figure 10: Eccentricity along the longitudinal crownline for self-weight plus horizontal displacements of the supports, (a) *Groin vault*, (b) *Vault with thicker ribs*

3.5. FEM analysis for self-weight and vertical relative translations of the piers and lateral walls

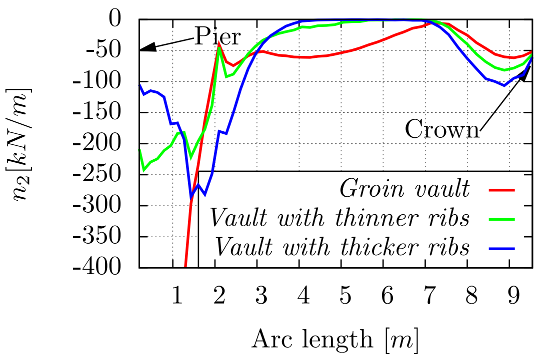

Figure 11: Principal compression membrane force along the groin, for self-weight plus a relative vertical support displacement of $20mm$

Figure 11 belongs to a 20 mm relative vertical displacement of boundary Γ_0 on both sides. The diagrams show how the minimal principal membrane force varies in the points of the shell along the diagonal groin. At about halfway between the crown and the pier the compression force becomes negligible, which means that the voussoirs are particularly endangered for sliding out.

Figure 12 (a,b,c) shows the minimum principal membrane force for the same displaced state. The difference among the three pictures is that the red domains, i.e. the regions of weak compression, are larger in the case of ribbed vaults.

Figure 13 (a,b,c) shows the mobilized friction ratio for the same displaced state. The red and dark blue regions are those where sliding would occur in a vault with a frictional constitutive model of Coulomb for the joints; again, the ribs increase these domains.

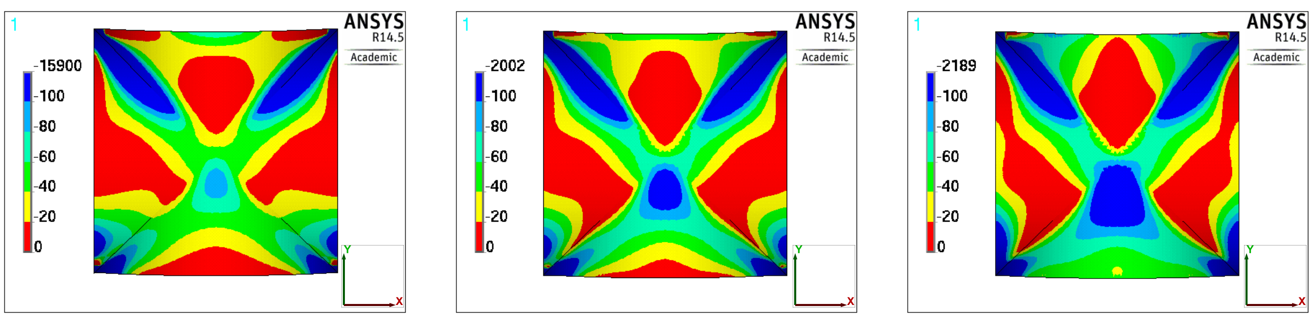

(a) (b) (c)

Figure 12: Magnitude of principal compression membrane force along the vault surface for self-weight plus a relative vertical support displacement of 20 mm, (a) *Groin vault*, (b) *Vault with thinner ribs*, (c) *Vault with thicker ribs*

The increasing danger of sliding is explained by the presence of the ribs making the structure stiffer; in order to adjust itself to the modified geometry corresponding to support displacements, frictional sliding of the vault becomes more likely.

3.6. Overview of the FEM results

The linear finite element simulatons yielded rather questionable results. The well-known longitudinal hinging crack along the crownline was correctly predicted, and the stress-distributing role of the ribs hypothesized by Heyman was also pointed out. The ribbed structures behaved in a more rigid manner so they seemed to be more vulnerable for sliding than the unribben vault. However, otherwise the simulated behaviour did not sufficently match the pathology of cross vaults known in engineering practice; Sabouret's cracks, for instance, could not be predicted. Thus a numerical modelling technique capable of following separation of blocks, sliding, and large displacements of the voussoirs, would be more appropriate. Such an analysis will be introduced in Section 4.

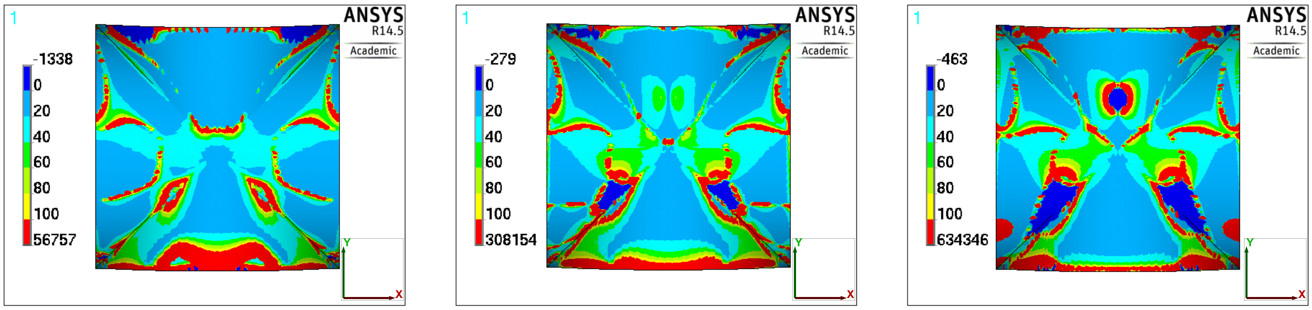

(a) (b) (c)

Figure 13: Magnitude of the ratio of mobilised fricion, $f[\%]$, along the vault surface for self-weight plus a relative vertical support displacement 20 mm, (a) *Groin vault*, (b) *Vault with thinner ribs*, (c) *Vault with thicker ribs*

4. Discrete element analysis

4.1. The mechanical model

4.1.1. Fundamentals of 3DEC

The discrete element analysis was done with the help of the 3DEC code of Itasca CG. In this software discrete elements may have any convex or concave polyhedral shape, and they are made deformable by being divided into uniform-strain tetrahedral finite elements whose constitutive relations have to be specified by the user. The nodes of the tetrahedra have only translational degrees of freedom, unlike the nodes in the FEM analysis in Section 3. The basic unknowns of the analysis are the nodal translations: their increments are calculated step by step along the given series of small but finite time intervals, and at any stage of the simulated loading process the uniform strain tensor of any tetrahedron can be determined from them, which then gives the stress tensor through the constitutive relations. The nodal translations are calculated with the time integration of Newton's force-acceleration law. The mass of a node is defined to be proportioned to the volume of the Voronoi cell around that node, and different forces (e.g. gravity, contact forces expressed by the adjacent elements) may act on the Voronoi cell of the node.

The contacts between the discrete elements may have two different roles in the DEM model of a masonry structure, depending on the intention of the user. The first option is that the contacts represent some kind of a mortar layer between the voussoirs, with a finite thickness in reality. In this case the material parameters of the contacts in 3DEC express the deformability characteristics of the mortar layer, e.g. stiffness and fracture criteria. The second option (the one that was used in the present study) is suitable for those structures where the contacts are dry or there is only a negligible layer of mortar between the voussoirs. In this case a contact exists in 3DEC if a node belonging to the boundary of a discrete element gets into the interior of another element. Though in reality such an inter-penetration is impossible, in 3DEC a constant distributed contact force occurs in this case in the neighbourhood of the penetrated node. The intensity of the normal component of this distributed force is proportional to the magnitude of the inter-penetration (i.e., relative normal translation of the node and of the surface point through which it entered the other block); the normal stiffness jkn should be infinite in reality, and a very large value in the 3DEC model. The intensity of the tangential component is proportional to the relative translation of the node and the surface point on the other block; if frictional sliding does not occur, in reality this relative translation should also be zero. Thus, the tangential stiffness jks should approximate the infinity in the 3DEC model. The Coulomb limit sets a limit on the tangential force component according to a user-defined frictional angle ϕ in the model. The friction angle ϕ characterises the real behaviour of the contacts, while jkn and jks are numerical parameters influencing the model behavoiur. The jkn and jks values should theoretically be infinitely large, but the larger they are, the shorter is the allowed time step length, leading to increasing computational time. (In the present study the stiffness values were chosen according to the detailed analysis of this question published in Simon and Bagi, [13].)

4.1.2. Geometry

The vault models were prepared according to the same reference surface introduced in Section 2.1 and applied also for the FEM modelling in Section 3. This reference surface determined the middle plane of the approximately brick-shaped blocks forming the masonry shell, while at its groins and along its four semicircular sides the elements forming the ribs were placed. In order to specify the corners of the bricks of the shell (see Figure 1), first the reference surface was approximated with rectangles of edges in hoop and meridional directions. In the next step at the straight sections the corners were defined perpendicularly to the reference surface. Finally, half of the shell thickness was measured inwards and the other half outwards, in order to find the corners of the bricks along the intrados and the extrados. The bricks were truncated where having contacts with the ribs or at the groins (see Figure 14). According to [14], the connection between two elements meeting at an unribbed groin was made perfectly rigid such that the two truncated elements were "glued together" (Figures 14 (a,b)), while the ribs and the adjacent truncated elements were in Coulomb-type frictional contact (Figures 14 (c,d)).

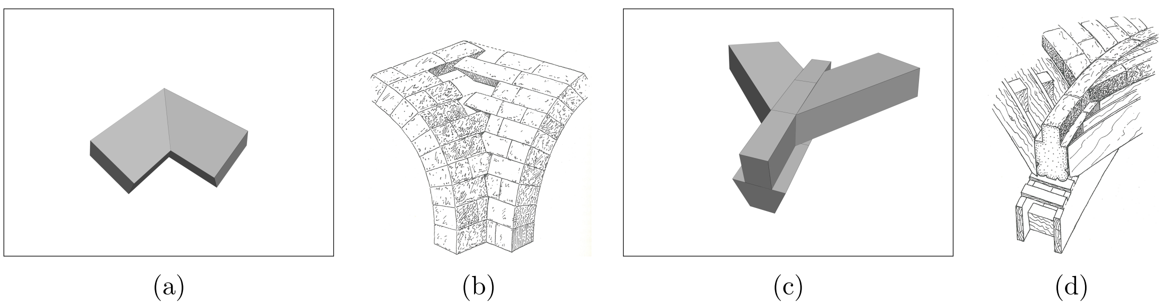

Figure 14: Discrete element model of the neighbourhood of the groin: (a) Joined blocks along the groin, unribbed vault model, (b) real formation of the groin in an unribbed vault according to [14], (c) truncated blocks in the shell at the rib in ribbed vault model, (d) real formation of the neighborhood of the diagonal rib according to [14]

The shape of the elements forming the ribs was already described in Section 2.1. All contacts were planar. The tetrahedral subdivision of the blocks into finite elements was done in such a way that the mesh density increased near the groins. The maximum edge size of the tetrahedra, l_{max}, varied according to the following rule:

$$l_{max}[\text{mm}] = 50 + 0.75d, \tag{3}$$

where d denotes the distance from the nearest groin in meter.

4.1.3. Material properties

The material properties of the blocks and joints of the models are summarized in Section 2. The blocks were linearly elastic and isotropic with infinite strength; the joints followed the Coulomb model for friction and had a very large normal ($jkn = 10^3$ GPa) and shear stiffness ($jks = 10^3$ GPa), to express that deformations are carried by the blocks while contacts deform only if they separate or slide.

4.1.4. Loads and boundaries

The simulated load cases were the same as in the FEM investigations (self-weight with perfect geometry; self-weight plus outwards horizontal relative translation of the opposite piers and walls; self-weight plus vertical relative translation of opposite piers and walls). Figure 15 illustrates boundary regions where different displacement components of the nodes were prescribed. Unlike in the FEM model, in 3DEC the nodes have translational degrees of freedom only, so the corresponding translation components of the nodes along different boundary regions were set to zero for self-weight (see Table 3; $d_h = d_v = 0$), or moved with a suitably chosen velocity history in the case of support displacement investigations.

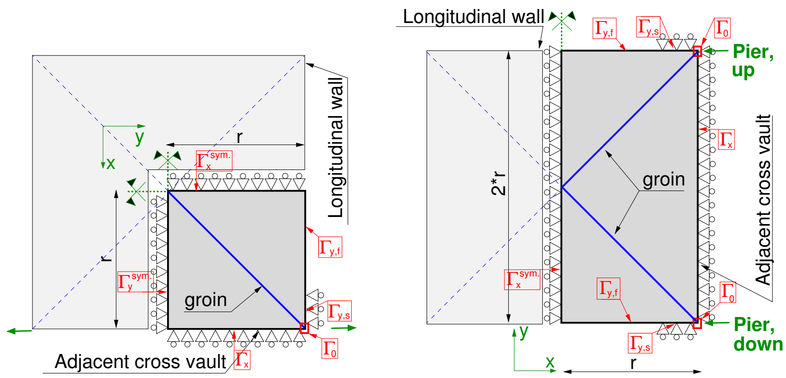

(a) (b)

Figure 15: Reduced size DEM models in order to take advantage of the symmetry, (a) horizontal relative displacement, (b) vertical relative displacement

Boundary	u	v	w
Γ_0	0	d_h	d_v
Γ_x	0	-	-
$\Gamma_{y,s}$	-	d_h	-
$\Gamma_{y,f}$	-	-	-
$\Gamma_x^{sym.}$	0	-	-
$\Gamma_y^{sym.}$	-	0	-

Table 3: Boundary conditions in the discrete element simulations, self-weight, self-weight plus prescribed horizontal (d_h) or vertical support displacements (d_v)

In order to take advantage of the symmetries of the analyzed problems, only the half of the cross vault was simulated in the case of vertical support displacements, and only the quarter in the horizontal displacements (see Figure 15). The nodes along the straight horizontal artificial boundaries $\Gamma_x^{sym.}$ and $\Gamma_y^{sym.}$ were fixed against horizontal translations perpendicularly to the boundary (Table 3).

The support displacements were produced in a quasi-static manner. During 1 mm steps the boundaries were moved with a very low velocity (decreasing from 12 m/s to zero), and after reaching a total translation of 1 mm, all moving boundaries were fixed and the structure was carefully balanced (i.e., timestepping was continued until the ratio of maximal unbalanced force and the largest contact force decreased below 10^{-5}) before starting to move the supports again.

4.1.5. The analyzed characteristics

Ribs

First a local frame (ξ, η, ζ) was assigned to the centroids of the contact surfaces between the voussoirs (see Fig. 16). In the contacts of the blocks forming the ribs, axis ζ was perpendicular to the groin line and was parallel to the vertical plane of the groin. Axis ξ was coincident to the outwards normal direction of the contact surface.

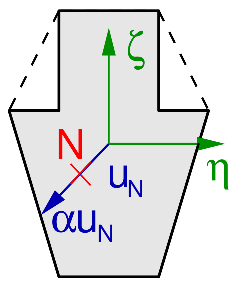

Figure 16: The local coordinate system and the eccentricity of the compression force resultant in a contact in the rib

In the contacts of the blocks of the ribs, axis η was normal to the plane of the rib (see Figure 16). Contacts between a block of the shell and another block in the rib were not considered in the analyzed characteristics.

The ratio of eccentricity, $e[\%]$, shows how close the point of action of the compression force N is to the convex boundary of the contact (the convex boundary is shown in dashed lines in Figure 16). Let u_N denote the distance of N from the centroid; $\alpha * u_N$ is the total distance from the centroid to the convex boundary, measured along the same direction. The eccentricity ratio is

$$e[\%] = \pm\frac{1}{\alpha}100, \tag{4}$$

where a positive or negative sign is also assigned: e is positive if N acts between the η axis and the extrados (a crack would open from below for an N acting outside the kernel of the contact); and negative if N is on the inner side of η (corresponding to crack opening from above). The ratio of eccentricity is not defined for a tensile N: the contacts can not resist tension in the model.

The mobilized friction ratio, $f[\%]$, relates the $\zeta - \textit{directed}$ shear resultant, $V_{\xi\zeta}$, to the Coulomb limit corresponding to the normal resultant N:

$$f[\%] = -\frac{V_{\xi\zeta}}{tan(\phi)N}100, \tag{5}$$

Note that the other shear component, $V_{\xi\eta}$, is neglected here.

Bricks of the shell

Consider a brick in the shell, and also consider its faces contacting the adjacent bricks. For a given face of the brick, define a frame (u,v,ζ), assigned to the center of the face in the following way. Axis u is normal to the face, pointing towards the adjacent brick. Axis ζ is normal to the reference surface (see Section 4.1.2). Finally, axis v is perpendicular to u and ζ, such that the plane (u,v) is tangent to the reference surface.

- Eccentricity ratio: $e[\%]$
  The resultant of the distributed normal force n_u acting on the face is usually eccentric in the sense that its point of action is at distance e_ζ from the reference surface. The absolute value of this distance can be calculated for all faces of the analyzed block, and the largest value gives the eccentricity parameter belonging to the block:

$$e[\%] = \max_{\text{(faces of the block)}} \left(\frac{e_\zeta}{h_w/2} * 100 \right), \tag{6}$$

- Mobilized friction ratio: $f[\%]$
  Let $q_{u\zeta}$ denote the ζ-directed component of the resultant of the distributed tangential force acting on a face of the analyzed block. Comparing this component (the out-of-plane shear) to the magnitude of the normal resultant n_u the out-of-plane mobilized friction coefficient can be calculated and related to the possible maximal value, $\tan(\phi)$. Considering all faces with the neighbours of the analyzed block, the largest value can be selected:

$$f[\%] = \max_{\text{(faces of the block)}} \left(\frac{q_{u\zeta}}{tan(\phi)(-n_u)} 100 \right), \tag{7}$$

- Magnitude of a hinging crack or separating crack: c^{hin}, c^{sep}[mm]
  As shown in Figure 17, a contact may be cracked either in such a way that the two blocks remain in contact (Figure 17 (a)), or in such a way that the two blocks completely separate from each other (Figure 17 (b)). In both cases, the largest relative normal translation of the points of the face of the adjacent block is selected to characterize the magnitude of crack opening. They are denoted by c^{hin} and c^{sep}, respectively (let the value of c^{hin} be defined, positive if the crack opens from below and negative if the crack opens from above). Next, the faces of the block are all analyzed, and the face with the largest absolute value is chosen again to be assigned to the block.

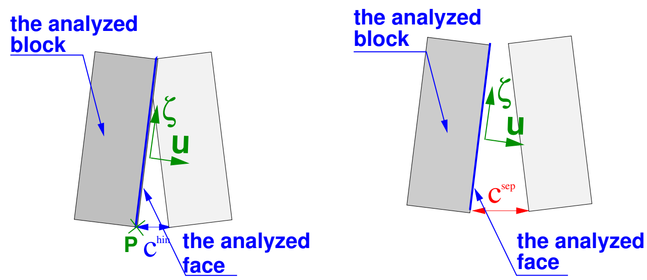

(a) (b)

Figure 17: Definition of the magnitude of (a) hinging cracks, (b) separating cracks

- Principal membrane forces
  A local frame (ξ, η, ζ) can be assigned to any point of any brick of the masonry shell, in the same way as it was described in Section 3.1. When analysing a given brick, consider the points of the straight section going through its centroid perpendicularly to the reference surface. By integrating normal stress components σ_ξ and σ_η along this line, membrane forces n_ξ and n_η are received; doing the same for in-plane shear stresses $\tau_{\xi\eta}$ gives membrane shear force $q_{\xi\eta}$. From these values principal membrane forces and their directions can be determined. The compressive principal membrane force and its distribution along the shell provides a good representation of how the loads are carried by the shell.

4.2. Self-weight investigations

4.2.1. Forces and displacements in the masonry shell

The different hypotheses on the "flow of compression" in cross vaults has been the subject of severe debates since Willis [3]. The membrane force trajectories shown in Figure 18 (for self-weight), and in the next sections (for self-weight plus support displacements) aim at providing a contribution to this debate.

The DEM simulations show that with perfect geometry and no support displacements the major compression trajectories are arranged in most of the ribbed and unribbed vaults in a similar way as those found by Alexander et al [6] for Gothic cross vaults on elastic basis, and those in version (c) of Block and Lachauer [15], giving best performance by TNA. The compression trajectories are mostly directed towards the piers, particularly in the vicinity of the diagonal groin. The dominant load-carrying direction is along the groin, independently of the presence of the ribs. However, this is not the case around the lower part of boundary $\Gamma_{y,s}$, where the lateral wall is slightly separated from the transversal barrel.

A disturbed region can be seen here in which the compressions nearly disappear, so the vault is particularly vulnerable for local failure, above this region (in the neighbourhood of the separated lateral wall) the trajectories correspond to a series of separate arches, standing parallel to the wall, each carrying its own weight.

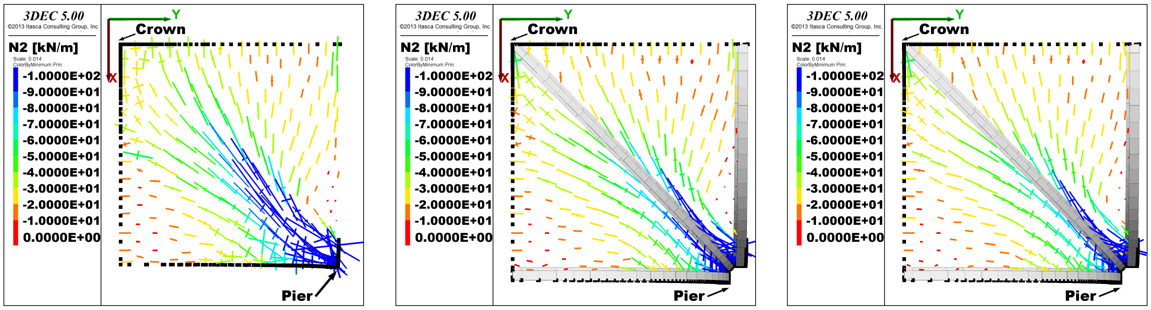

(a) (b) (c)

Figure 18: The membrane force trajectories for self-weight, (a) *Groin vault*, (b) *Vault with thinner ribs*, (c) *Vault with thicker ribs* (the ribs are also plotted)

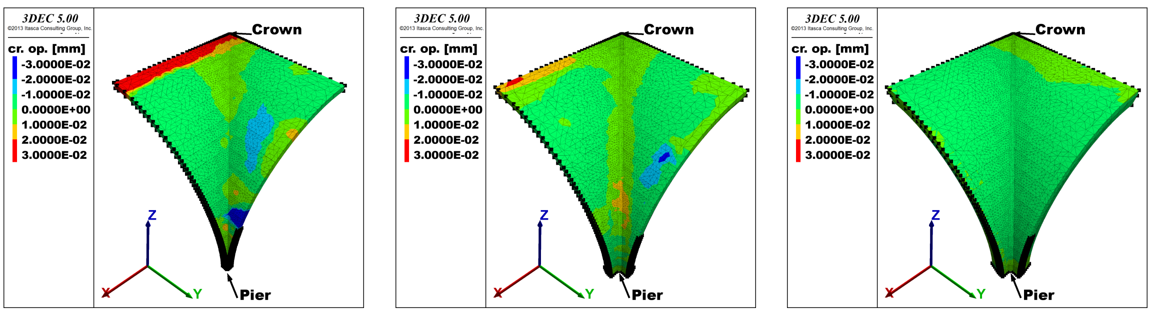

(a) (b) (c)

Figure 19: Hinging crack magnitude in the masonry shell for self-weight: (a) *Groin vault*, (b) *Vault with thinner ribs*, (c) *Vault with thicker ribs*

Figure 19 (a,b,c) illustrates the magnitude of hinging cracks for self-weight. Blue domains along the longitudinal crown line correspond to crack initation from below; in the yellow and red domains (in the transversal barrels) the cracks open from above. The ribs definitely decrease the crack magnitudes.

In Figure 20 (a,b,c) the separating crack magnitudes can be seen. Separation mostly occurs in the neighborhood of the free lateral boundary, and these cracks slightly smaller in the lack of ribs.

In general, hinging cracks are smaller while separating cracks are larger in the presence of the ribs; however, in every case the cracks are very small, about the order of 0.01 mm.

Figure 21 shows that the eccentricity of normal forces is surprisingly large already for self-weight with perfect geometry. Red domains are regions where the blocks have at least one face on which the compressive resultant force nearly reaches the intrados or the extrados. More detailed analysis (see Section 4.3 below) revealed that, indeed, horizontal support displacements cause hinging cracks to occur along the crown line corresponding to the red domains along the top of the longitudinal barrel, while the red domains across the transversal barrel are those regions where Sabouret's cracks initiate. The ribs decrease these domains: the eccentricities are smaller for thicker ribs.

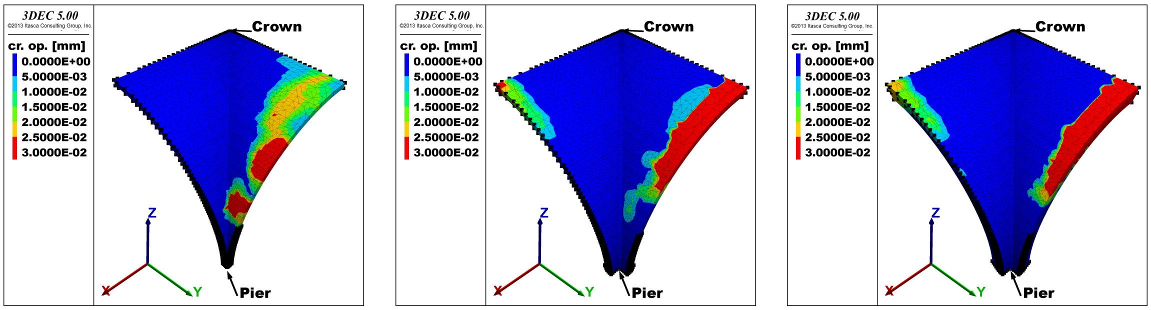

(a) (b) (c)

Figure 20: Magnitude of separating crack in the masonry shell for self-weight: (a) *Groin vault*, (b) *Vault with thinner ribs*, (c) *Vault with thicker ribs*

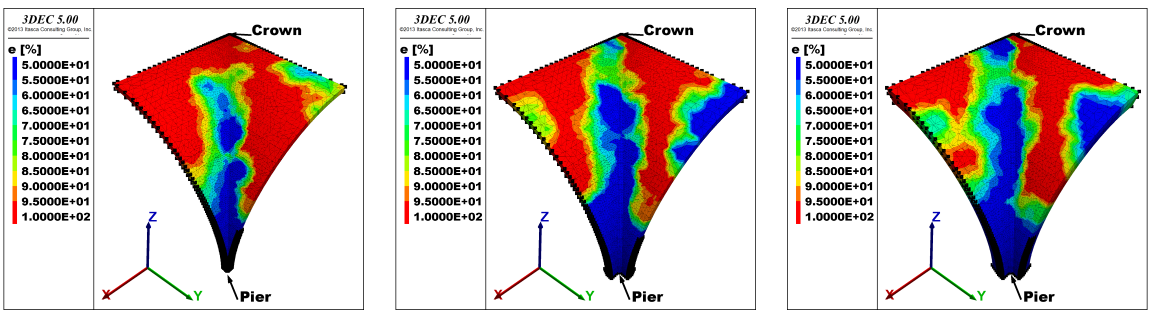

(a) (b) (c)

Figure 21: Magnitude of eccentricity in the masonry shell for self-weight: (a) *Groin vault*, (b) *Vault with thinner ribs*, (c) *Vault with thicker ribs*

4.2.2. Forces and deformations in the diagonal rib

Figure 22 (a,b,c) presents the magnitude of the compression force, the ratio of mobilized friction, and the eccentricity ratio along the rib, measured along the arch starting from the pier in the corner and running until the crown. Though the compression is large at the pier and then starts to decrease as proceeding upwards, the tendency changes when arriving at the neighbourhood of the disturbed region, and a local maximum is reached at about $25-30\%$ of the arc length. For a structure with thick rib this local maximum is even higher than the force at the pier. Above this region, the compression monotonically decreases until the crown.

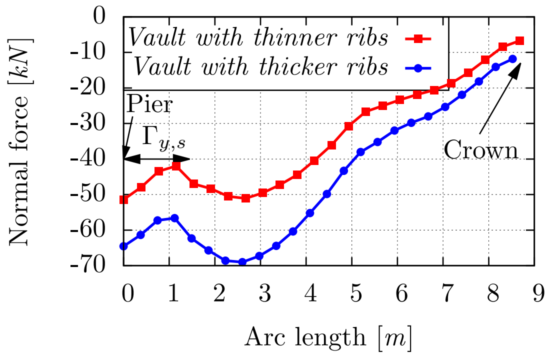

(a)

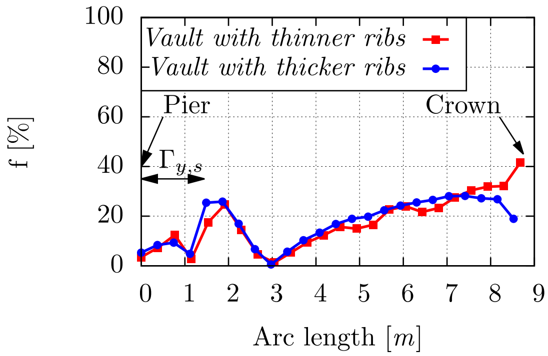

(b)

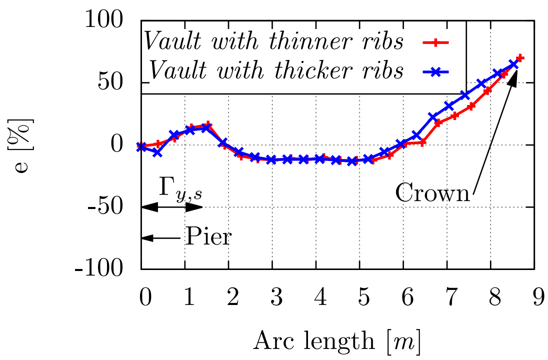

(c)

Figure 22: State characetristics of the ribs: (a) Compression force resultant, (b) Ratio of mobilized friction, (c) Ratio of eccentricity of the compression force

The ratio of mobilized friction (Fig. 22 (b)) is very far from 100% along the whole rib for both thicknesses, though the effect of the disturbed region can also be noticed here.

The ratio of eccentricity (Fig. 22 (c)) is also far from 100%, though it is not negligible near the crown. Positive values outside the bounded area mean that hairline cracks open up from below, on the intrados; negative values correspond to cracks opening from the extrados. Similar phenomenon was described by Barthel [4].

4.3. Horizontal support displacements

4.3.1. Forces and displacements in the masonry shell

In the range of small outwards displacements of supports Γ_0 and $\Gamma_{y,s}$ the membrane force trajectories (Figures 23 (a,b,c)) are rather similar to those seen for the case of fixed supports (Figure 18); the main difference is that the membrane forces are, in general, smaller than for fixed supports. The membrane forces gradually decrease with increasing small displacements. This is in agreement with the increasing compression in the ribs (see below in Section 4.3.2, Figure 28). Indeed, the principal compressional directions in Figures 23 (b) and (c) point more directly towards the ribs in the vicinity of the ribs: the ribs carry an increasing portion of the self-weight. In addition, the disturbed region around the top of boundary $\Gamma_{y,s}$ becomes more apparent with increasing displacements.

Distribution of the internal forces in the shell for large displacements the becomes rather different. The membrane force trajectories (Figures 24 (a,b,c), belonging to 200 mm outwards relative translation of the supports) reveal that a longitudinal, strongly compressed zone is formed along the crownline. With ribs, the compression trajectories change their direction even more significantly around the diagonal rib: except from the top of the vault, the characteristic direction of largest compression becomes nearly perpendicular to the rib.

The ratio of mobilized friction (figure not attached) reaches 100% only in a very small region of the unribbed structure even for large displacements; on the ribbed structures, however, these domains are definitely larger, particularly in the case of a thicker rib. The conclusion can be drawn that since the ribbed structures are more rigid, they adjust themselves to the support displacements by more significant sliding and separation.

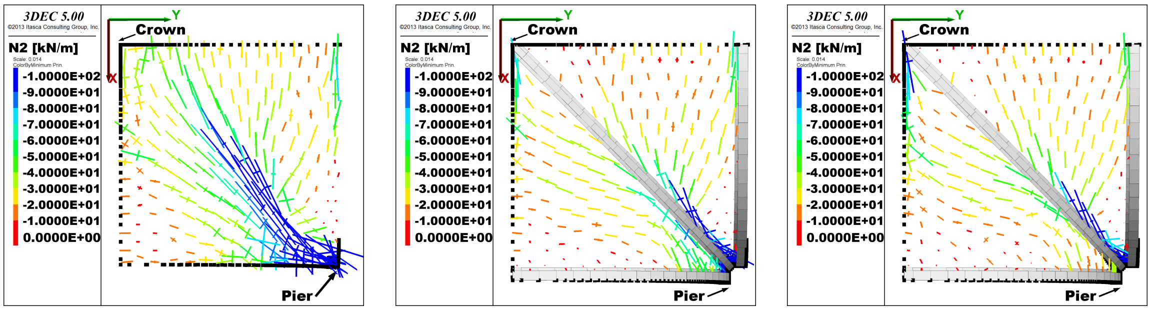

(a) (b) (c)

Figure 23: The membrane force trajectories for self-weight plus a relative horizontal support displacement of 10 mm, (a) *Groin vault*, (b) *Vault with thinner ribs*, (c) *Vault with thicker ribs* (the ribs are also plotted)

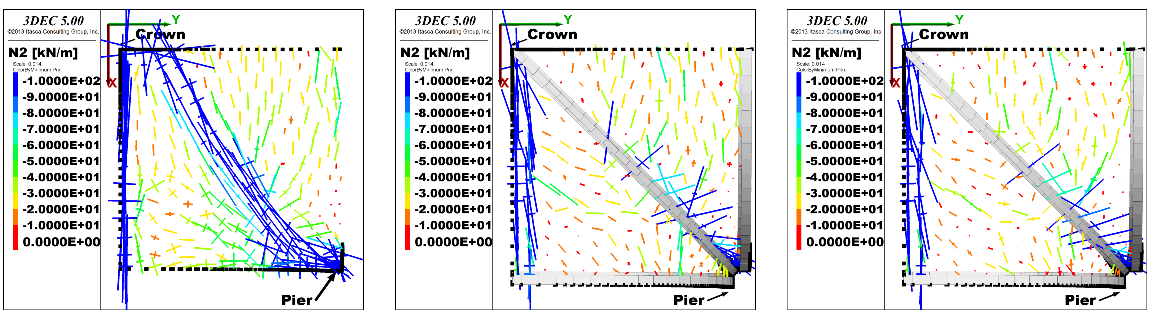

(a) (b) (c)

Figure 24: The membrane force trajectories for self-weight plus a relative horizontal support displacement of 200 mm, (a) *Groin vault*, (b) *Vault with thinner ribs*, (c) *Vault with thicker ribs* (the ribs are also plotted)

The hinging and separating cracks are shown for a 200 mm outwards relative translation of the supports in Figures 25 (a,b,c) and 26 (a,b,c). In all cases the usual pathology of cross vaults (e.g., Heyman [16]; Creazza et al [17]; Theodossopoulos and Sinha [18]) can clearly be recognised: a longitudinal crackline opens up from below along the crownline, and another one from above, clozer to the pier. In the ribbed structures the regions of significant contact separation (red domains in Figure 26) are more dominant than in the unribbed structure: in addition to the separation of the shell from the lateral wall, Sabouret' cracks (parallel to the walls) can also be seen.

This result, i.e. that a strongly compressed region was formed along the crownline, was unexpected. This phenomenon can be explained by the separation crack pattern nearby the crown, see Figure 26. For large horizontal support displacements the crown was not supported in the hoop direction so an internal thrust line with large pressure forces evolved in the longitudinal direction. This phenomenon was investigated deeply, but is not detailed here.

4.3.2. Forces and deformations in the diagonal rib

Figure 28 (a-f) illustrates how the compression force, the ratio of mobilized friction and the eccentricity ratio vary with increasing horizontal separation of the lateral boundaries of the vault, in the case of thinner

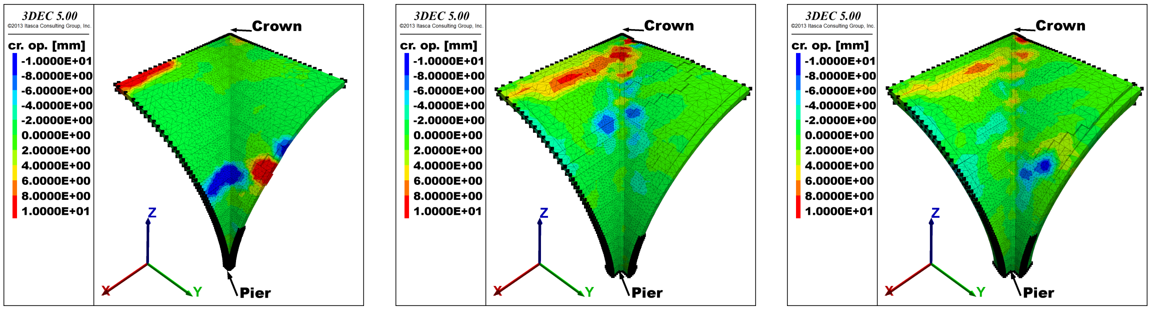

(a) (b) (c)

Figure 25: Hinging crack magnitude in the masonry shell for self-weight plus a relative horizontal support displacement of 200 mm: (a) *Groin vault*, (b) *Vault with thinner ribs*, (c) *Vault with thicker ribs*

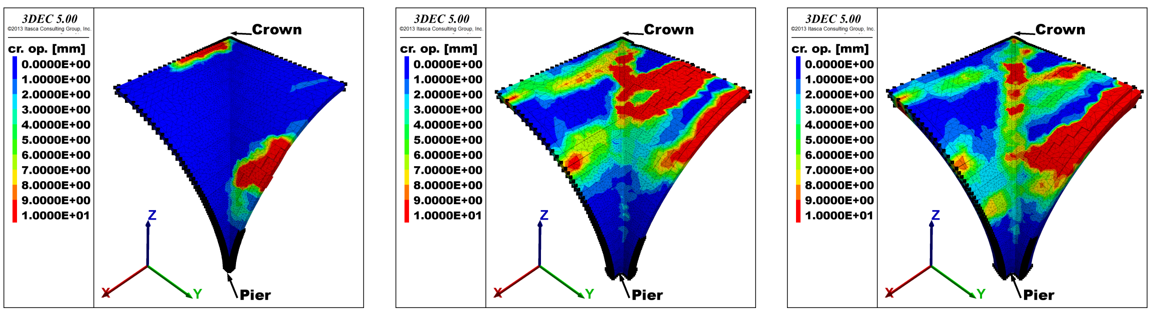

(a) (b) (c)

Figure 26: Separating crack magnitude in the masonry shell for self-weight plus a relative horizontal support displacement of 200 mm: (a) *Groin vault*, (b) *Vault with thinner ribs*, (c) *Vault with thicker ribs*

and thicker ribs. The different diagrams within the same figure correspond to different magnitudes of support displacements.

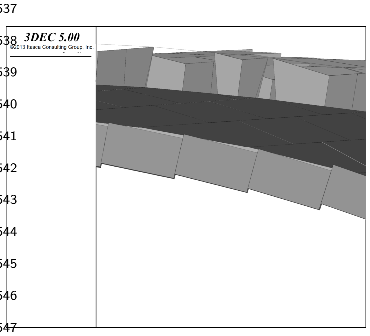

Figure 27: Sliding of the voussoirs in the diagonal rib, thinner rib

The most important experience provided by these diagrams is that the range of support displacements can be divided into "small" displacements meaning that the force characteristics are sensitive to slight increments of the displacements (relative translations) of approximately 0.2%, and to "large" displacements where further incremental motions do not cause significant modifications of the internal forces any longer. Normal force diagrams (Fig. 28 (a,b)) show that with increasing translations the rib forces mostly increase around the pier and in the neighborhood of the disturbed region. The ratio of mobilized friction (Fig. 28 (c,d)) reaches 100% at a relative displacement of about $0.15 - 0.20\%$ of the span; for both thicknesses the contacts in the upper region of the rib slide in the way shown in Figure 27.

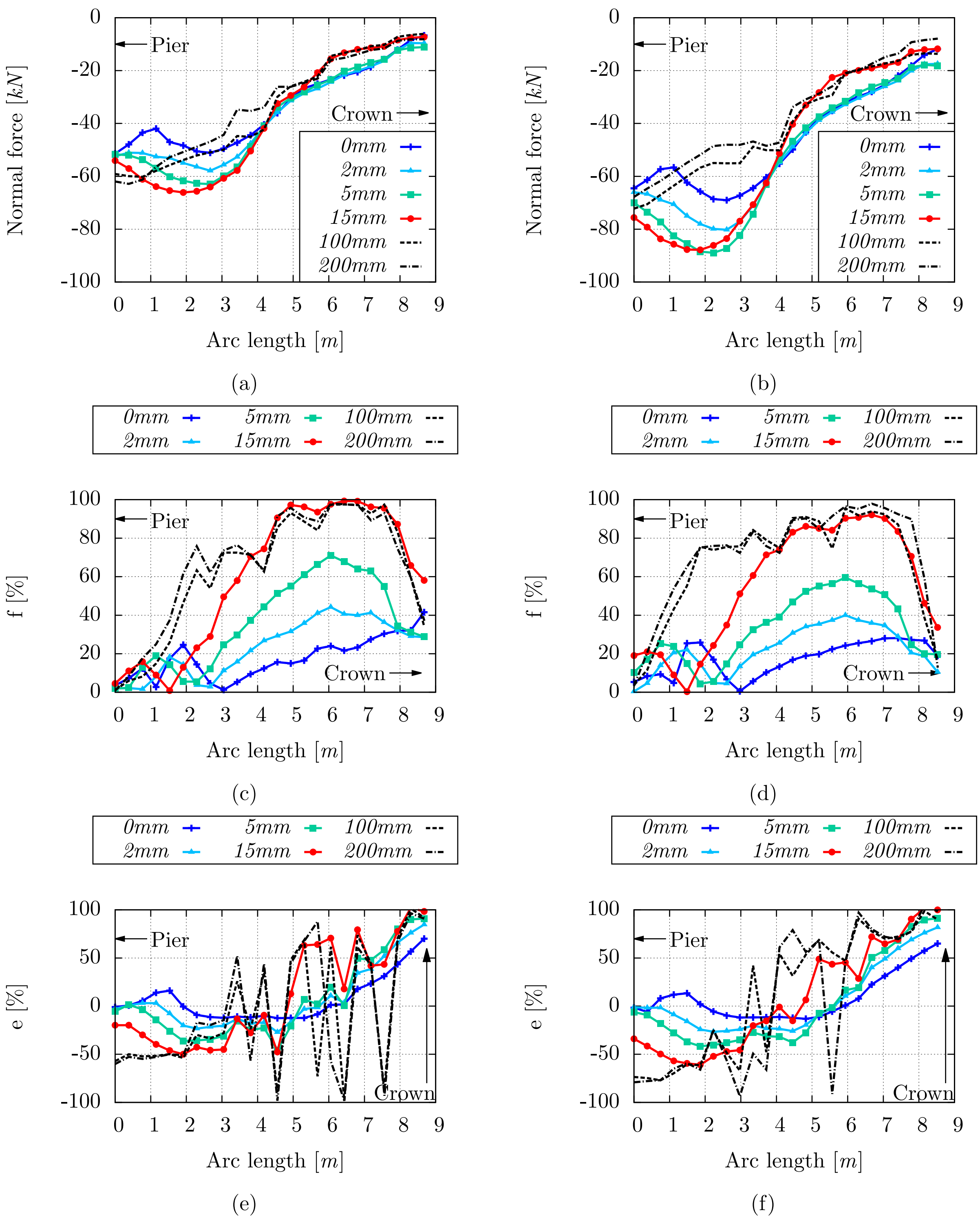

Figure 28: State characteristics of the ribs for self-weight plus different horizontal support displacements: (a) Compression force resultant in the case of thinner ribs, (b) Compression force resultant in the case of thicker ribs, (c) Ratio of mobilised friction in the case of thinner ribs, (d) Ratio of mobilised friction in the case of thicker ribs, (e) Ratio of eccentricity of the compression force in the case of thinner ribs, (f) Ratio of eccentricity of the compression force in the case of thicker ribs

4.4. Vertical support displacements

4.4.1. Forces and displacements in the masonry shell

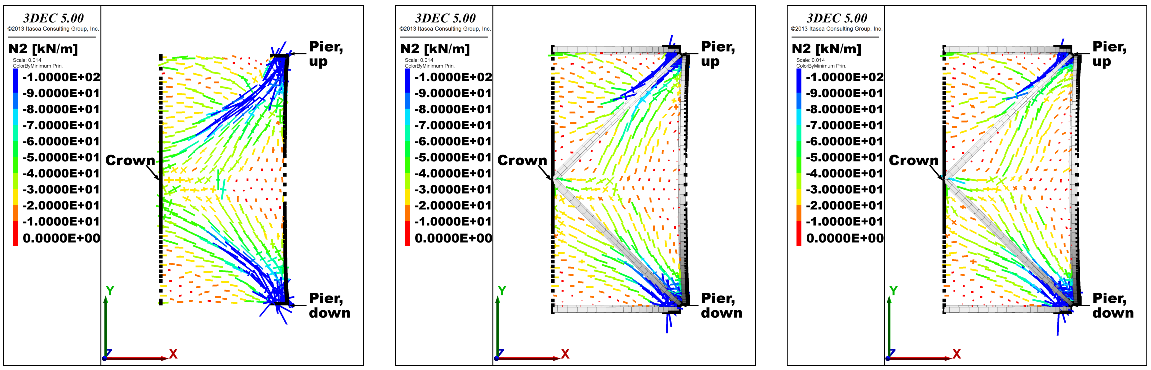

(a) (b) (c)

Figure 29: Membrane force trajectories for self-weight plus a relative vertical support displacement of 10 mm: (a) *Groin vault*, (b) *Vault with thinner ribs*, (c) *Vault with thicker ribs* (the ribs are also plotted)

Figure 29 shows the membrane force trajectories in the masonry shell, for a relative vertical displacement of 0.1% of the span. The basic difference between the unribbed and ribbed vaults are that forces are larger without ribs; the thicker the ribs are, the smaller the membrane forces become. For ribbed vaults (Figs. 29 (b) and (c)) membrane forces are smaller around the pier moving upwards than at the pier moving downwards. Direction of the principal compressive forces are almost perpendicular to the rib moving upwards, but nearly parallel to the rib moving downwards. Similarly to the horizontal support displacements, a strongly compressed zone along the crownline can also be recognized here, particularly for ribbed vaults.

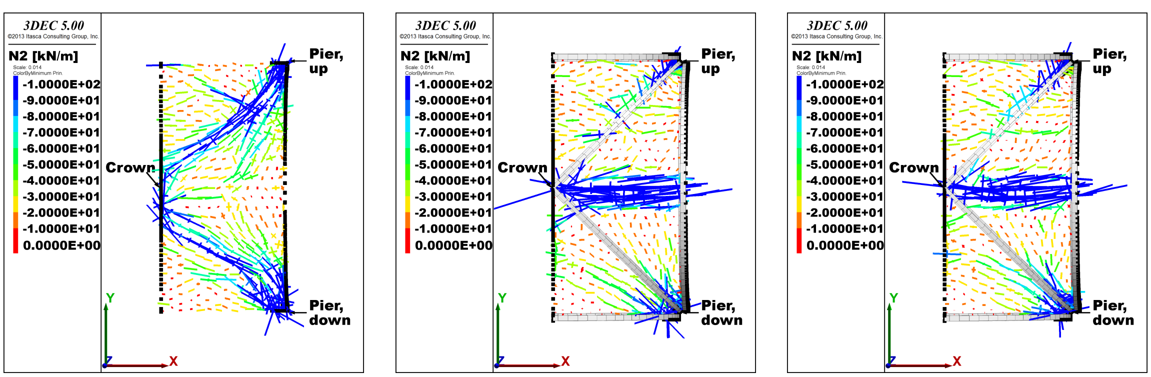

(a) (b) (c)

Figure 30: Membrane force trajectories for self-weight plus a relative vertical support displacement of 200 mm: (a) *Groin vault*, (b) *Vault with thinner ribs*, (c) *Vault with thicker ribs* (the ribs are also plotted)

As the displacements increase, the distribution of the internal forces in the shell significantly change, particularly in the ribbed vaults. Figure 30 presents the membrane force trajectories for a vertical relative displacement of 2% of the span. Two basic differences can be recognized between the unribbed and the ribbed vaults. The first one is that a strongly compressed longitudinal zone is formed in the ribbed structures along the crownline, like also experimented with horizontal displacements, while this zone is nearly completely missing in the unribbed vault. The other difference is that the neighbourhood of the diagonal groins carries large compressions in the unribbed vault as if substituting the missing ribs, while in the case of ribbed structures the masonry shell transfers the loads on the ribs and hence the forces in the shell are significantly smaller. (The same phenomenon was seen in the case of horizontal displacements in Figure 24.)

Figure 30 showed that large longitudinal forces evolved in longitudinal direction like at horizontal displacements for the same reasons. An apparent difference can be seen between the unribbed and ribbed vaults: without ribs, the compression is small and the compressed zone is not developed yet. Further analysis (not presented here in detail) revealed, however, that further increase of relative vertical displacements led to the formation of a compressed zone for the unribbed vault too.

The ratio of mobilised crosswise friction is shown in Figure 31. There is only a small domain where it is close to 100% for the unribbed vault: this domain surrounds the pier which moves upwards, as if the neighborhood of moving boundaries Γ_0 and $\Gamma_{y,s}$ would punch through the shell. The vaults with thin and with thick ribs have definitely more extended sliding or nearly-sliding regions. In general, the ratio of mobilized friction is larger on the upwards moving side than on the downwards moving side. The explanation may again be given by the fact that the ribbed structures are stiffer so these structures can adjust themselves to the support displacements with the help of cracking and contact sliding.

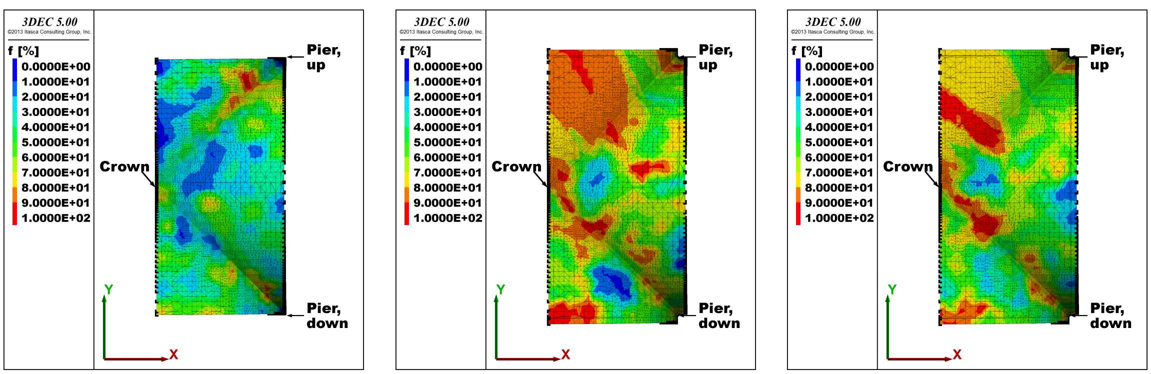

(a) (b) (c)

Figure 31: Magnitude of mobilised friction ratio in the masonry shell for self-weight plus a relative vertical support displacement of 200 mm: (a) *Groin vault*, (b) *Vault with thinner ribs*, (c) *Vault with thicker ribs*

The deformations of the masonry shells are explained by Figures 32 and 33 (hinging and separating crack magnitudes, respectively), again for a relative vertical displacement of 2% of the span. In the unribbed structure (Figs 32 (a) and 33 (a)) the transversal barrel is separated from the longitudinal wall on the upwards moving side, and two longitudinal lines of hinges appear in the longitudinal barrel: one along the downwards side of the crownline opens from below, and one near the upwards pier opens from above. In the behaviour of the ribbed vaults separation is more dominant than hinging. Interpreting Figures 32 (b-c) and 33 (b-c) together with the force trajectories in Figure 30 (b-c), it can be seen that in the transversal barrels in the neighbourhood of the diagonal ribs the voussoirs of the shell are separated from each other and lead the forces down to the ribs as individual arches. Significant separating cracks appear in the part of the shell moving upwards and at both lateral walls.

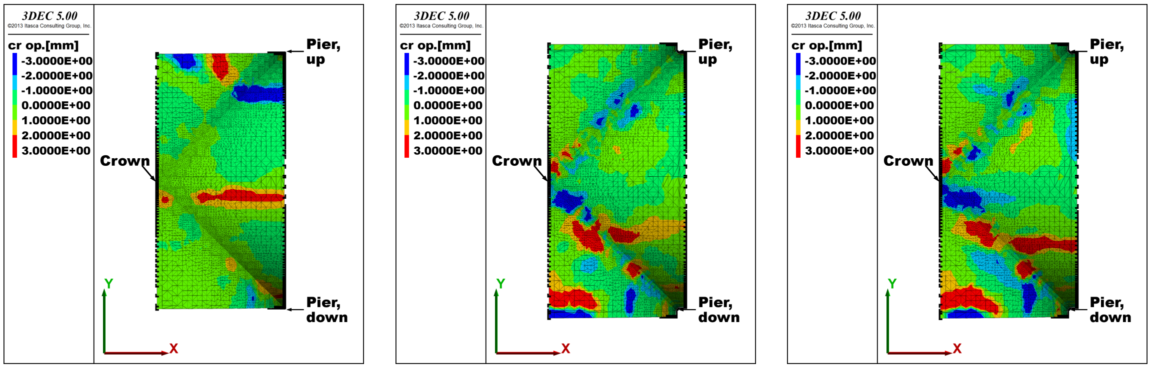

(a) (b) (c)

Figure 32: Hinging crack magnitude in the masonry shell for self-weight plus a relative vertical support displacement of 200 mm: (a) *Groin vault*, (b) *Vault with thinner ribs*, (c) *Vault with thicker ribs*

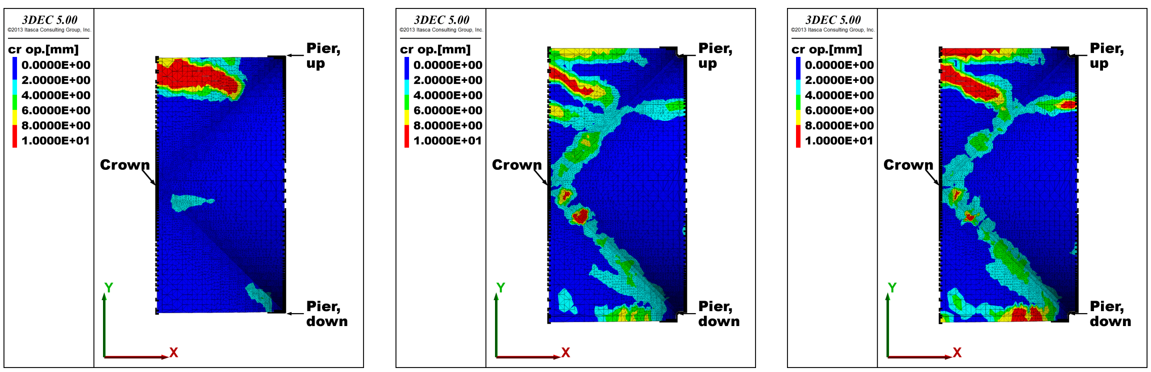

(a) (b) (c)

Figure 33: Separating crack magnitude in the masonry shell for self-weight plus a relative vertical support displacement of 200 mm: (a) *Groin vault*, (b) *Vault with thinner ribs*, (c) *Vault with thicker ribs*

4.4.2. Forces and deformations in the diagonal rib

Figure 34 presents the magnitude of normal force, the ratio of mobilized friction and the ratio of eccentricity of the normal force in the rib, respectively. On each diagram the horizontal axis represents the line that starts from the pier moving upwards, proceeds along the rib, reaches the crown in the middle, then turns to the adjacent rib and finally reaches the pier moving downwards. Different lines belong to different magintudes of relative vertical support displacements in each figure.

The compressive forces (Fig. 34 (a,b)) are, in general, larger in the rib moving upwards than on the downwards side. Forces gradually change with increasing displacements; at about 15 mm (0.15% of the span) a state is reached which remains approximately unchanged for further displacements. Thicker ribs carry larger forces, which is in agreement with Figure 29 showing that forces in the masonry shell are smaller in the case of the thicker ribs.

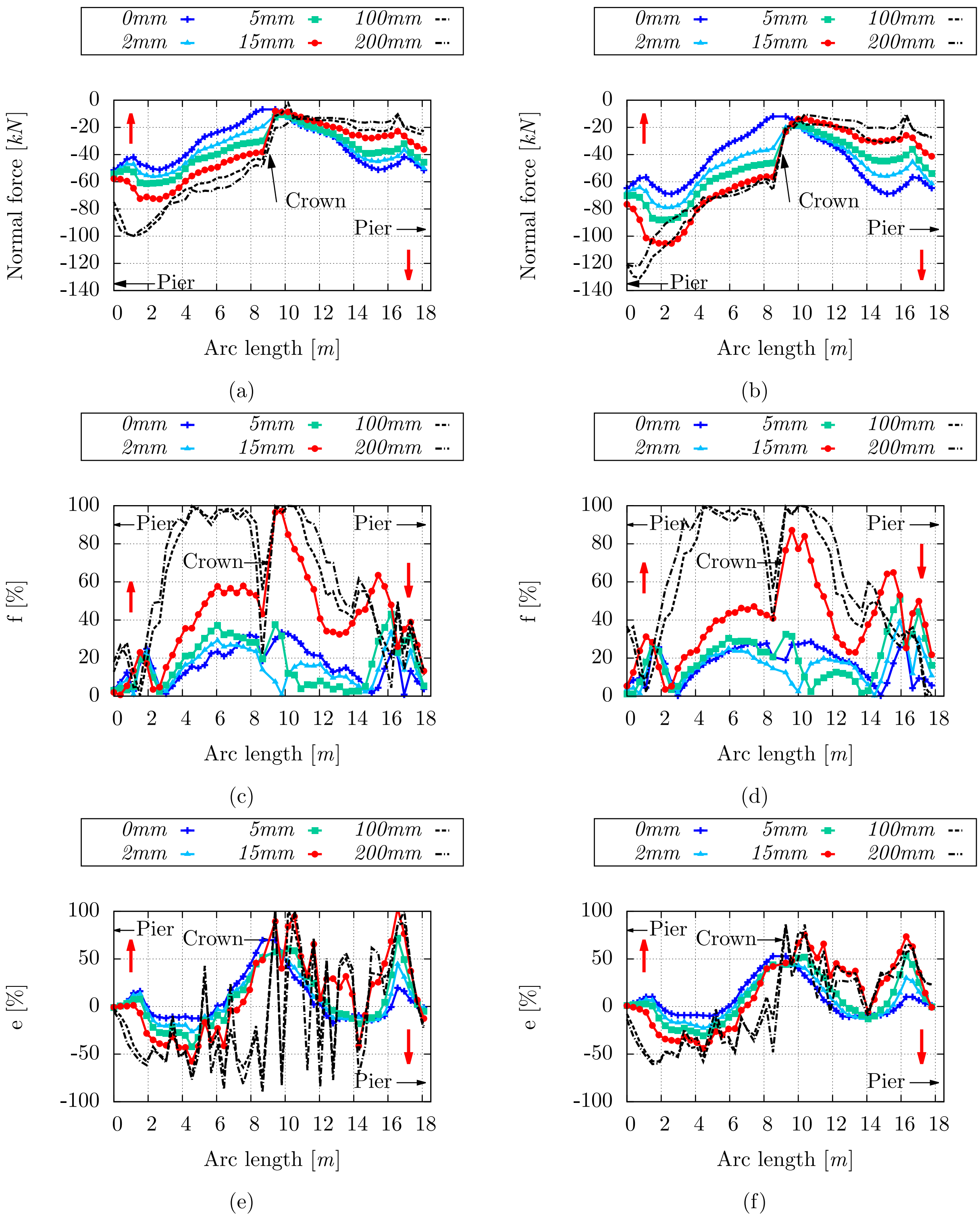

Figure 34: State charactristics of the ribs for self-weight plus different vertical support displacements: (a) Compression force resultant in the case of thinner ribs, (b) Compression force resultant in the case of thicker ribs, (c) Ratio of mobilized friction in the case of thinner ribs, (d) Ratio of mobilized friction in the case of thicker ribs, (e) Ratio of eccentricity of the compression force in the case of thinner ribs, (f) Ratio of eccentricity of the compression force in the case of thicker ribs

The diagram on the ratio of mobilized friction (Fig. 34 (c,d)) shows that until a relative displacement of 15 mm no sliding happens. At 15 mm the contacts at the crown are nearly sliding; at 100 mm (1.0% of the span) characteristic sliding zones of the ribs occur, and they remain unchanged for increasing displacements.

Figure 34 (e,f) shows how the eccentricity of the compressive force varies along the ribs. Initially the eccentricity is largest around the crown, but even here it is far from 100%. As the displacements increase, a hinge forms near the pier moving downwards. At a relative vertical translation of 15 mm additional hinges appear near the crown in the rib moving downwards.

4.5. Overview of the DEM results

Characteristic crack patterns given by the discrete element simulations for outwards horizontal support displacements are in good agreement with practical experiences on real cross vaults: longitudinal hinge lines, Sabouret's cracks and separation from the lateral walls can clearly be recognised. Consequently the results related to the internal forces of the different cross vaults can also be considered reliable, definitely more than the FEM results.

The membrane force trajectories are fan-like for fixed supports and for small support displacements, apart from a disturbed region around the point of the lateral wall where it is separated from the edge of the transversal barrel. For increasing support displacements a more and more dominant compressed zone develops in the shell along the longitudinal crownline. In the case of ribbed vaults the principal compression around the groin approaches the direction perpendicular to the groin and an increasing part of the weight of the shell is transferred to the ribs.

An advantageous effect of the ribs is that they reduce large stresses occuring in the shell along the groins and near the piers.

"Small" and "large" support displacements can be distinguished for unribbed as well as for ribbed structures. While the displacements are small, additional horizontal or vertical displacements cause significant modifications in the internal force system: the forces are sensitive to small increments of the displacements. Further on, after reaching about 0.15% of the span for horizontal and 0.20% for vertical relative support displacements, the characteristic sliding and cracking zones are formed and they remain approximately unchanged for further displacement increments, analyzed until the magnitude of 2% of the span in the present paper.

Ribbed vaults behave more rigidly, which leads to more extensive cracking and sliding at the same level of prescribed displacements than vaults without ribs.

5. Conclusions

- The discrete element simulations give a definitely more reliable insight into the mechanical behaviour of ribbed and unribbed cross vaults than linear FEM simulations.
- Ribs reduce the stress peaks around the piers in the corner, and with increasing support displacements they carry an increasing part of the weight of the masonry shell. The ribs reduce forces in the shell, particularly along the groins.
- Ribbed structures are more rigid than unribbed vaults, and as a result, they are more exposed to cracking and sliding.
- For increasing support displacements a strongly compressed zone (partly separated from the adjacent shell) develops along the longitudinal line of crown.
- Until a "small" relative support displacement of about 0.15 − 0.20% of the span the internal force system varies signifiantly. Dominant cracks gradually open up, sliding zones are formed, and the structure develops an internal state which then remains unchanged for further ("large") displacements of the supports.

Acknowledgement

The authors acknowledge and thank the Itasca Education Partnership for the generous contribution of software and technical support to this research. Financial support from OTKA 100770 project is greatly acknowledged.

AppendixA. Analysis of the lateral boundary

Assuming no-tension joints and no external buttresses, in a general cross vault of a long nave the transversal barrel and the lateral wall are only partially connected: as the wall slightly bends outwards because of the horizontal pressure exerted by the vault, the upper region of the lateral edge of the transversal barrel becomes separated from the wall. The reliable modelling of the mechanics of a cross vault requires a reasonable approximation of the length along which the connection still exists. Such an estimation was the aim of the DEM simulations presented in the Appendix.

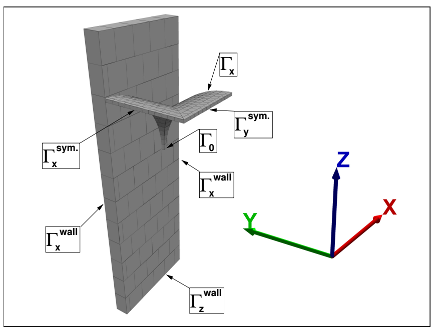

Figure A.35: The complex masonry system for the analysis of boundary Γ_y

Figure A.35 shows the complex masonry system analysed in the simulations. Taking advantage of the symmetry, only a quarter of the cross vault was modelled. The pier supporting the lowest block of the vault was replaced by boundary Γ_0. The free height of the wall (measured vertically from the bottom of the lowest blocks of the wall, until the corner of the cross vault at boundary Γ_0) was 6, 9 and 12 m in different tests. Wall thickness was also treated as a changing parameter: widths of 100, 120, 140 and 160 cm were applied. The radius of the barrels was set to $5m$, the same as throughout the whole paper. The lowest nodes of the wall, boundary Γ_z^{wall} were fixed against any translation, while boundary Γ_0 of the cross vault was supported in x and z (longitudinal and vertical) directions. Boundaries $\Gamma_x^{sym.}$ and $\Gamma_y^{sym.}$ of the vault (reflecting the symmetries in the displacement behaviour) were the same as in Section 4, while the vertical boundaries of the wall, boundaries Γ_x^{wall} were free, these conditions are summarized in Table A.4. (Note that with these boundary conditions the self-weight can produce a slight deviation between the vertical translation of the neighbouring nodes in the vault and in the wall, if permitted by the frictional resistance. The role of the lateral walls in the DEM models was to provide only a lateral (but no vertical) support.)

All contacts were of type Coulomb, and the material parameters were the same as in the whole paper.

Indices from 1 to 20 were assigned to the blocks on the lateral edge of the transversal barrel vault (see Figure A.36).

Starting from the initial, undeformed and unloaded state, the self-weight of the structure was "switched on", and the model was balanced. Then the resultant compressive forces exerted by the wall on the lateral blocks of the transversal barrel were determined. Figure A.37 illustrates the case of free height of 12 m and wall thickness of 160 cm: the indices shown in Figure A.37 are seen here along the horizontal axis, while the magnitude of the lateral compressive forces is shown vertically. Similar analysis was done for all geometries. The results for a vault with thinner ribs are summarized in Table A.5.

Boundary	u	v	w
Γ_0	0	-	0
Γ_x	0	-	-
$\Gamma_{y,s}$	-	0	-
$\Gamma_{y,f}$	-	-	-
$\Gamma_x^{sym.}$	0	-	-
$\Gamma_y^{sym.}$	-	0	-
Γ_x^{wall}	-	-	-
Γ_z^{wall}	0	0	0

Table A.4: Boundary conditions applied in the analysis of boundary Γ_y

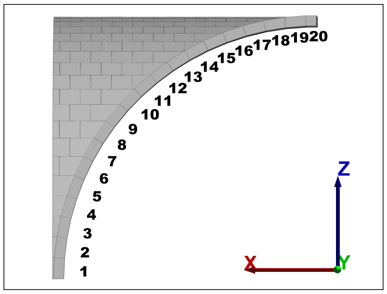

Figure A.36: Block indices along the contact with the lateral wall

The results show that in every case the lowest block was exposed to the largest lateral compression. Proceeding then upwards, slightly depending on the specific data of the models that influence the bending stiffness of the wall, the next $4-5$ blocks still received considerable compression from the wall. Above them, the blocks either carried negligible compression only, or became completely separated from the wall and a free boundary of the transversal barrel was formed.

Consequently, the DEM simulations in the paper were done in such a way that the effect of the wall along the lowest quarter of the arc length was represented by a boundary $\Gamma_{y,s}$ resisting y-directed translations, and above this, boundary $\Gamma_{y,f}$ was free without any prescribed displacement.

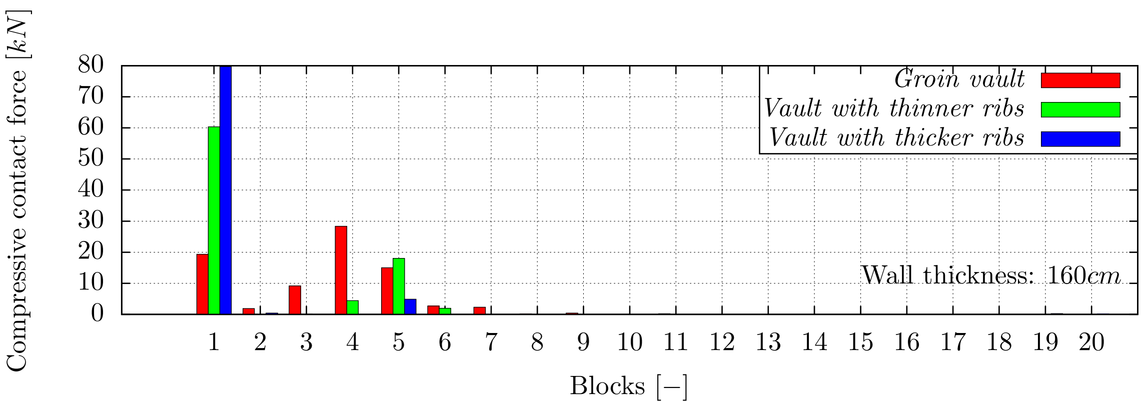

Figure A.37: Compression exerted by the wall on the blocks of the vault, free height is 12 m, wall thickness is 160 cmm

Wall height	Wall thickness	Compressive contact force [kN]																			
		1	2	3	4	5	6	7	8	9	10	11	12	13	14	15	16	17	18	19	20
6 m	100 cm	55	0	0	13	8	1	0	0	0	0	0	0	0	0	0	0	0	0	0	0
	120 cm	44	1	2	15	14	10	0	0	0	0	0	0	0	0	0	0	0	0	0	0
	140 cm	35	4	4	15	13	17	4	0	0	0	0	0	0	0	0	0	0	0	0	0
	160 cm	34	5	4	16	13	17	4	0	0	1	0	0	0	0	1	0	0	0	0	0
9 m	100 cm	60	0	0	9	6	0	0	0	0	0	0	0	0	0	1	0	0	0	0	0
	120 cm	55	0	1	11	6	0	0	0	0	0	0	0	0	0	1	0	0	0	0	0
	140 cm	51	0	2	16	6	0	0	0	0	0	0	0	0	0	0	0	0	0	0	0
	160 cm	46	0	3	18	11	3	0	0	0	0	0	0	0	0	0	0	0	0	0	0
12 m	100 cm	73	0	0	2	0	0	0	0	0	0	0	0	0	0	0	0	0	0	0	0
	120 cm	73	0	0	3	2	1	0	0	0	0	0	0	0	0	0	0	0	0	0	0
	140 cm	65	0	0	10	7	0	0	0	0	0	0	0	0	0	0	0	0	0	0	0
	160 cm	60	0	0	4	18	0	2	0	0	0	0	0	0	0	0	0	0	0	0	0

Table A.5: Compressive forces exerted by the wall on the blocks of the crosswise barrel: *Vault with thinner ribs*

[1] P. Fuentes, S. Huerta, Islamic domes of crossed-arches: Origin, geometry and structural behavior, in: 6th International Conference on Arch Bridges, Fuzhou, Japan, 2010, pp. 346–353.

[2] S. Huerta, The debate about the structural behaviour of gothic vaults: From viollet-le-duc to heyman, in: Proceedings of the Third International Congress on Construction History, Cottbus, Germany, 2009, pp. 837–844.

[3] R. Willis, Remarks on the Architecture of the Middle Ages, especially of Italy, Cambridge Pitt Press, Cambridge, 1835.

[4] R. Barthel, Tragverhalten gemauerter Kreuzgewölbe, Universität Karlsruhe, Karlsruhe, 1993.

[5] J. Heyman, The Stone Skeleton. Structural Engineering of Masonry Architecture, Cambridge University Press, Cambridge, 1995.

[6] K. Alexander, R. Mark, J. Abel, The structural behaviour of medieval ribbed vaulting, Journal of the Society of Architectural Historians 36 (1977) 241–251.

[7] P. Block, J. Ochsendorf, Thrust network analysis: A new methodology for three-dimensional equilibrium, Journal of the International Association for Shell and Spatial Structures 48 (2007) 198–204.

[8] R. Livesley, Limit analysis of structures formed from rigid blocks, International Journal of Numerical Methods 12 (1978) 1853–1871.

[9] R. Livesley, The collapse analysis of masonry arch bridges, Conference on Applied Solid Mechanics 12 (1992) 261–274.

[10] A. Orduña, P. Lourenço, Part i: Torsion failure on frictional joints and limit analysis formulation, Solids and Structures 42 (2005) 5140–5160.

[11] D. D'Ayala, E. Tomasoni, Study on structural behaviour of masonry vaults: limit state analysis with finite friction, VI International Conference on Structural Analysis of Historical Constructions (2008) 5140–5160.

[12] Á. Török, Geology for Engineers, Műegyetem press, Budapest, 2007.

[13] J. Simon, K. Bagi, Discrete element analysis of masonry domes with oval plan, submitted to: International Journal of Solids and Structures – (2014) –.

[14] J. Fitchen, The Construction of Gothic Cathedrals A Study of Medieval Vault Erection, Clarendon Press, Oxford, 1961.

[15] P. Block, L. Lachauer, Three-dimensional (3d) equilibrium analysis of gothic masonry vaults, International Journal of Architectural Heritage 8 (2014) 312–335.

[16] J. Heyman, Chronic defects in masonry vaults: Sabouret's cracks, Momentum 26 (02) (1983) 131–141.

[17] G. Creazza, R. Mateazzi, A. Saetta, R. Vitaliani, Analysess of masonry vaults: A macro approach based on three dimensional damage model, Journal of Structural Engineering (2002) 646–654.

[18] D. Theodossopoulos, B. Sinha, Structural safety and failure modes in gothic vaulting systems, in: 8th International Seminar on Structural Masonry, Istanbul, Turkey, 2008, pp. –.